Available online at www.sciencedirect.com
ScienceDirect
Trans. Nonferrous Met. Soc. China 35(2025) 3342−3356
Transactions of Nonferrous Metals Society of China
www.tnmsc.cn

Origin of high strength and good ductility of TiH_2-based powder metallurgy titanium alloy with discontinuous lamellar structures

Hai-rui ZHANG[1,2], Hong-zhi NIU[3], Chao YANG[4], Nan XIANG[1,2], De-liang ZHANG[3], Fu-xiao CHEN[1,2]

1. School of Materials Science and Engineering, Henan University of Science and Technology, Luoyang 471023, China;
2. Provincial and Ministerial Co-construction of Collaborative Innovation Center for Non-ferrous Metal New Materials and Advanced Processing Technology, Luoyang 471023, China;
3. School of Materials Science and Engineering, Northeastern University, Shenyang 110819, China;
4. Shanghai Key Laboratory of Advanced High-temperature Materials and Precision Forming, School of Materials Science and Engineering, Shanghai Jiao Tong University, Shanghai 200240, China

Received 21 February 2024; accepted 9 August 2024

Abstract: A unique discontinuous lamellar microstructure of titanium alloys consisting of lamellar colonies at prior β-Ti grain boundaries and internal interwoven α-laths is prepared by a TiH_2-based powder metallurgy method. The α-variants get various crystallographic orientations and become discontinuous during vacuum annealing at 700 °C. Remarkably, nanoscale phase δ-TiH compound layers are generated between α-laths and β-strips, so that dislocations are piled up at the $\alpha/\delta/\beta$ interfaces during tensile deformation. This leads to dislocation slips being confined to individual α-laths, with different $\langle a \rangle$ slips and particularly pyramidal $\langle c+a \rangle$ slips being activated. The efficiency of wavy slip is promoted and the work hardening rate is enhanced. Finally, the combined effect of dispersed micro-shear bands and lath distortions is considered contributive for alleviating the stress concentration at grain boundaries, resulting in a high-promising synergy of enhanced ultimate tensile strength of 1080 MPa and good elongation to fracture of 13.6%.

Key words: TiH_2-based powder metallurgy; discontinuous lamellar microstructure; interfacial δ-TiH phase; tensile properties; deformation behavior

1 Introduction

Titanium and its alloys exhibit preeminent properties such as excellent corrosion resistance, good creep resistance, low density and high specific strength, being important structural metallic materials in the aerospace, navigation, biomedical and chemical industries [1]. Powder metallurgy (PM) is an effective approach to realize short process and cost-effective production of titanium alloys and their components, which has attracted considerable attention worldwide [2−4]. The titanium alloys prepared via traditional blended elemental (BE) PM usually have lamellar microstructure with thick and straight grain boundary α (α_{GB}) phases due to the necessary high sintering temperature [5]. The trade-off between strength and ductility of traditional PM titanium alloys has always been an issue for the widespread commercial applications [4]. Generally, when the oxygen content of traditional PM titanium alloys is above 0.35 wt.%, high yield strength but premature fracture at the prior β-Ti grain boundaries of the common lamellar microstructure will take place [6].

The process using TiH_2 powder instead of hydrogenated and dehydrogenated (HDH) Ti powder as feedstock to fabricate titanium alloys is

Corresponding author: Hai-rui ZHANG, Tel: +86-13842058301, E-mail: hairui_z@163.com
https://doi.org/10.1016/S1003-6326(25)66884-1

known as TiH_2-based PM, which has several unique advantages [7−9]. First, TiH_2 is inherently brittle and contributes to the densification of the powder compacts [10]. Second, 0.3 wt.% of hydrogen content effectively decreases the hot deformation resistance of titanium alloys due to the strong β-stabilization of hydrogen [11,12]. Third, apparent self-cleaning and volume shrinking effects are found to be induced by dehydrogenation reaction during powder sintering, accelerating the densification degree of the resulting alloy [4,13]. Fourth, some crystal lattice defects are introduced during dehydrogenation, which improves the solid-state diffusion abilities of Ti and alloying elements and promotes the alloying process of PM titanium alloys [14]. Finally, dehydrogenation process includes multi-stage phase transitions and brings about a refined microstructure for PM titanium alloys [15−17].

Unique microstructural characteristics have been achieved using TiH_2-based powder metallurgy, and these characteristics are different from those produced with HDH-Ti powder and those produced by conventional ingot metallurgy. A bimodal microstructure of Ti−0.38O containing equiaxed α grains and β-transformed (β_t) regions is fabricated by hot extrusion of high-energy mechanically-milled TiH_2 powder and following vacuum annealing [18]. Synchronously enhanced ultimate tensile strength (UTS, 932 MPa) and good elongation to fracture (EL, 26.2%) are obtained; in contrast, a wire arc additively manufactured Ti−0.37O alloy composed of acicular α-colonies has a low UTS of 730 MPa and low EL of 7.0% [19]. A discontinuous lamellar microstructure of Ti−6Al−2Sn−4Zr−2Mo−0.1Si−0.38O titanium alloy is produced by thermal mechanical consolidation of TiH_2-based powder compact. The initial regular lamellar microstructure gives rise to the EL as low as 5.5%. After inducing β_t to replace thin β layers, an impressive high EL of 13.0% is achieved [20]. By designing a discontinuous lamellar microstructure dominated by interwoven α-Ti laths and β fragments in Ti−6Al−4V−0.29O alloy, the EL reaches 10.0%. This is essentially attributed to the presence of various fine α-Ti variants with different crystallographic orientations [21]. It can be speculated that a proper microstructure design is the key to improve the ductility of high-oxygen titanium alloys via TiH_2-based PM method.

In addition, it is contradictory that titanium hydride particles are brittle and beneficial to powder metallurgy process but TiH-laths are not conducive to the ductility of PM titanium alloys. The EL of a PM pure titanium decreases from 16% to 3.5% due to the small amount of retained hydrides in the fine α-laths [22]. However, the EL increases from 3.5% to 12.0% by constructing heterogeneous structures within fine prior β grains of Ti−4Al−4Mo−4Sn−0.5Si−0.38O, although a small number of parallel nanosized needle-like titanium hydrides and long α_{GB} layers are retained [23]. Moreover, when titanium alloys are cooled from a high-temperature in single β-phase field, the α_{GB} regions are initially precipitated at the original β grain boundaries by diffusion-controlled planar growth [24]. Subsequently, Widmanstatten structures of parallel lamellar colonies (α_{WGB}) appear as allotriomorphs at the α_{GB} regions and grow inward the initial β grains [25]. The effect of the α_{WGB} regions on the mechanical properties of titanium alloys has recently been investigated [26,27]. When the α_{WGB} is partly replaced by interwoven α-lath structure, a high number density of interwoven α/β interfaces are formed. However, the tensile properties and the deformation behavior of high-oxygen PM titanium alloys with such a composite lamellar microstructure have less been studied.

In this study, a PM near-alpha Ti−3Al−2Zr−2Mo titanium alloy containing 0.36 wt.% oxygen and characterized by a composite lamellar microstructure consisting of grain boundary α_{WGB} and internal interwoven α-laths (α_{WI}) regions was fabricated by a TiH_2-based PM method involving powder compact, induction sintering, immediate hot extrusion and vacuum annealing. Interestingly, the α/β interfaces became discontinuous and a nanoscale interfacial FCC δ-TiH phase was found to generate between the α and β phases in the α_{WGB} regions during vacuum annealing. Subsequently, the corresponding origin of the enhanced strength and good ductility was discussed in detail. This work suggests a new strategy for the fabrication of PM titanium alloys with a combination of high strength and good ductility.

2 Experimental

The powder feedstock was composed of self-made TiH_2 sponge (hydrogen content ~4.1 wt.%),

AlMo60 master alloy particles, high-purity Al powder (<74 μm), and ZrH_2 powder (≤20 μm). The TiH_2 sponge particles were crushed by a planetary ball mill machine at a rotation speed of 300 r/min, and after milling for 5 min, an average powder size was 25 μm. The powder was passivated in the transition chamber of glove box to prevent self-ignition. After being mixed in a biconical mixer for 24 h, the TiH_2-based powder mixture of Ti−3Al−2Zr−2Mo was cold pressed in a steel die at a maximum pressure of 960 MPa and using a holding time of 5 min. Well-shaped powder compacts with dimensions of *d*53 mm × 52 mm were produced. The morphologies of the powder and green compacts as well as the elemental distribution mapping are shown in Fig. 1. The milled TiH_2-based powder mixture is irregular. The oxygen and nitrogen levels of the initial TiH_2 powder are measured to be 0.25 wt.% and 0.023 wt.%, respectively. The distributions of AlMo60 particles and Al, Mo, and Zr elements are uniform, and there is no aggregation in the green compact. As to the detailed illustration of the hot extrusion process, please refer to our previously published article [8]. The heating rate of induction sintering is about 80 °C/min, while that of vacuum sintering is set to be 10 °C/min. The sample after vacuum dehydrogenation annealing at 700 °C for 6 h is named as 700-PM-PE. For comparison, the same alloy's counterpart with an oxygen content of 0.43 wt.% and a regular lamellar microstructure prepared by vacuum sintering and hot forging is named as 700-PM-PF. The detailed description of the as-forged counterpart can be found in Ref. [28].

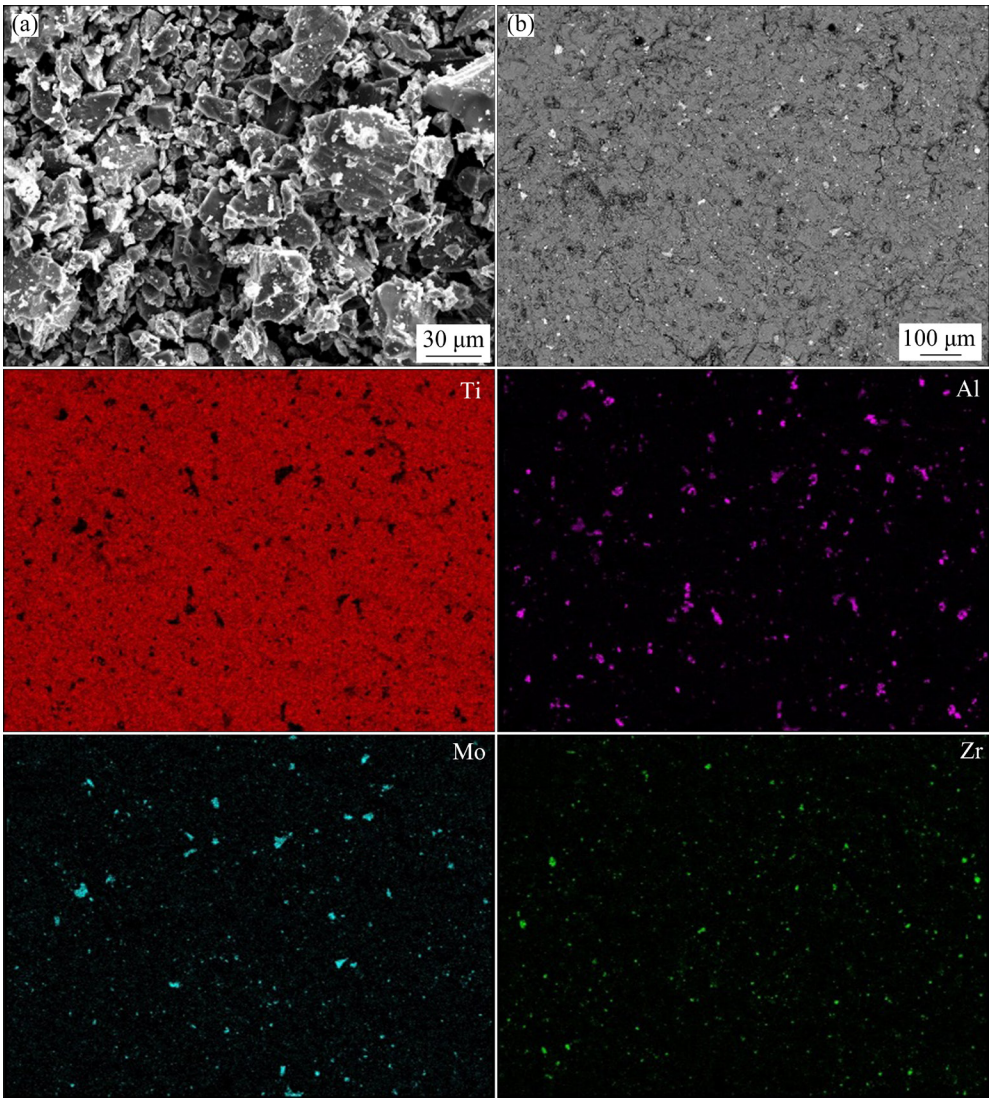

Fig. 1 Morphologies of blended elemental (BE) powder (a) and TiH_2-based mixture powder compact (b), with EDS maps of elements Ti, Al, Mo and Zr on fracture of powder compact

The real density of the PM titanium alloy sample was monitored using an electronic hydrometer (ETnAln, ET−320). The hydrogen and oxygen contents of the samples at different processing stages were measured by a Bruker oxygen−hydrogen analyzer (G8 GALILEO). Optical microscope (OM, ZEISS Axio Lab.A1), scanning electron microscopes (SEM, JSM−7001F and JSM−6510A), electron backscatter diffraction (EBSD), electron probe microanalyzer (EPMA, JXA−8530F), and transmission electron microscope (TEM, JEM−2100F) were used to characterize the microstructure. Phase constituents were detected by X-ray diffractometry (XRD, Smartlab (9), Rigaku) using a Cu K_α filtered ray scanning at a scanning speed of 6.0 (°)/min. EBSD specimens were prepared by standard metallographic preparation procedure followed by an electrolytic polishing with a solution of 6% perchloric acid + 34% butanol + 60% methanol at −30 °C and 25 V. EBSD data were collected by a symmetry detector equipped with a ZEISS Cross Beam 550 FIB/SEM system. TEM foils of 60 μm in thickness and 3 mm in diameter were prepared by mechanical polishing and twin-jet electron polishing with the same electrolytic polishing solution as that of EBSD samples.

Tensile tests were performed at room-temperature on a Shimadzu AG/X Plus 100 KN machine at an initial strain rate of 5.0×10^{-4} s^{-1}. Flat dog-bone shaped specimens with a gauge length of 15 mm and cross-sectional area of 3 mm × 2 mm were used for the tensile tests. The tensile direction is parallel to the extrusion direction. Three tensile samples under each state were tested to obtain average values of tensile properties with extensometer. Another specimen was measured by the macro digital image correlation (DIC) measurements equipped with VIC−3D software.

3 Results

3.1 Microstructural characteristics

The microstructure of the as-sintered samples with different sintering parameters is displayed in Fig. 2. The relative density of the sample by induction sintering at 1300 °C for 5 min is nearly 99.0%, being higher than that of the vacuum sintered sample (94.0%) [5]. There are almost no visible pores inside the induction sintered sample. Fine lamellar microstructure consisting of fine hydrogen-rich α (α(H)) or α-laths within different

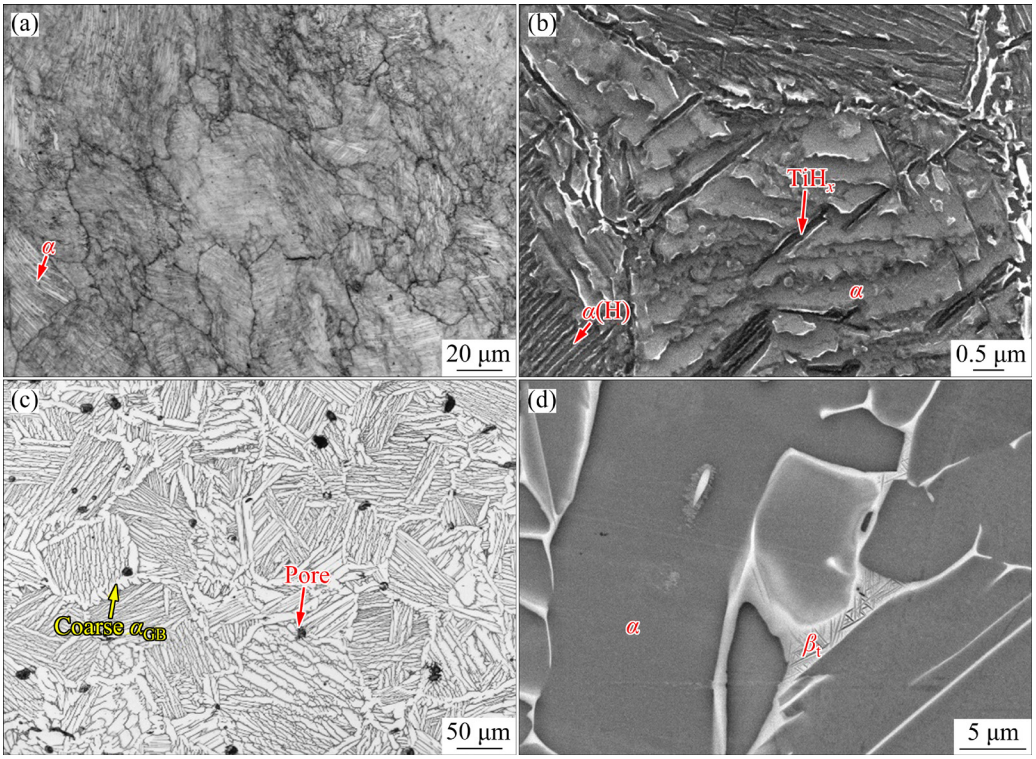

Fig. 2 OM (a, c) and SEM (b, d) images of sample induction heating sintered at 1300 °C for 5 min (a, b) and sample vacuum sintered at 1300 °C for 2 h (c, d)

sized prior β-grains is observed in the induction sintered sample, as shown in Fig. 2(a). The differences between α(H) and α-laths are mainly reflected in the width and contrast. The width of hydrogen-rich α(H) is smaller and the contrast of OM images is darker in α(H) laths, because hydrogen is a β-phase stabilizer. Therefore, the amount of fine α plates is considered to be α(H), except for a few broadened α-laths. The magnified image in Fig. 2(b) shows the presence of needle-like titanium hydrides (TiH_x) inside α-laths, as marked by the red arrow. Moreover, refractory Mo element is sufficiently present in the solid solution, and no enrichment zone is detected, although the preservation time at 1300 °C is only 5 min. This demonstrates that dissolved hydrogen atoms facilitate elemental diffusion and sintering densification. The grain boundary α phase of the induction sintered sample is discernible as a thin, curved layer. In contrast, a common α/β lamellar microstructure composed of thick α-laths and α_{GB} layers within uniform sized prior β-grains is obtained in the vacuum sintered sample, as shown in Figs. 2(c, d). Notably, the lath width of the induction sintered sample is only one-eighth that of the vacuum sintered sample.

Figure 3 illustrates the microstructural characteristics of the hot-extruded TiH_2-based rod. After hot extrusion, the grain size of prior β-grains is relatively homogeneous. The relative densities are increased to approximately 100% after hot deformation. The oxygen content is measured to be 0.36 wt.% and the hydrogen content remains at 0.21 wt.%, indicating that the dehydrogenation reaction is almost completed after induction sintering and immediate hot extrusion. The morphology of α_{GB} becomes blurred and the width is still much smaller than that of the vacuum sintered sample. Furthermore, parallel α lamellae (α_{WGB}) regions are primarily located around the original β grain boundaries, whereas α_{WI} regions containing interwoven α aciculae and β_t are detected inside the original β grains, as shown in Figs. 3(a, b). The co-existence of α_{WGB} and α_{WI} is considered to be related to the large cooling rate, i.e., more than 20 °C/min, after extrusion, as reported in Refs. [19,20].

After dehydrogenation annealing in vacuum at 700 °C for 6 h, the oxygen content of the 700-PM-PE sample remains almost constant, but the hydrogen content is decreased to 0.014 wt.%. Discontinuous α/β lamellar characteristics are generated in the α_{WGB} regions, as shown in Fig. 3(c). In addition, some β_t domains transform into a series of discontinuous fragments, accompanied by a slightly local broadening of the internal α aciculae

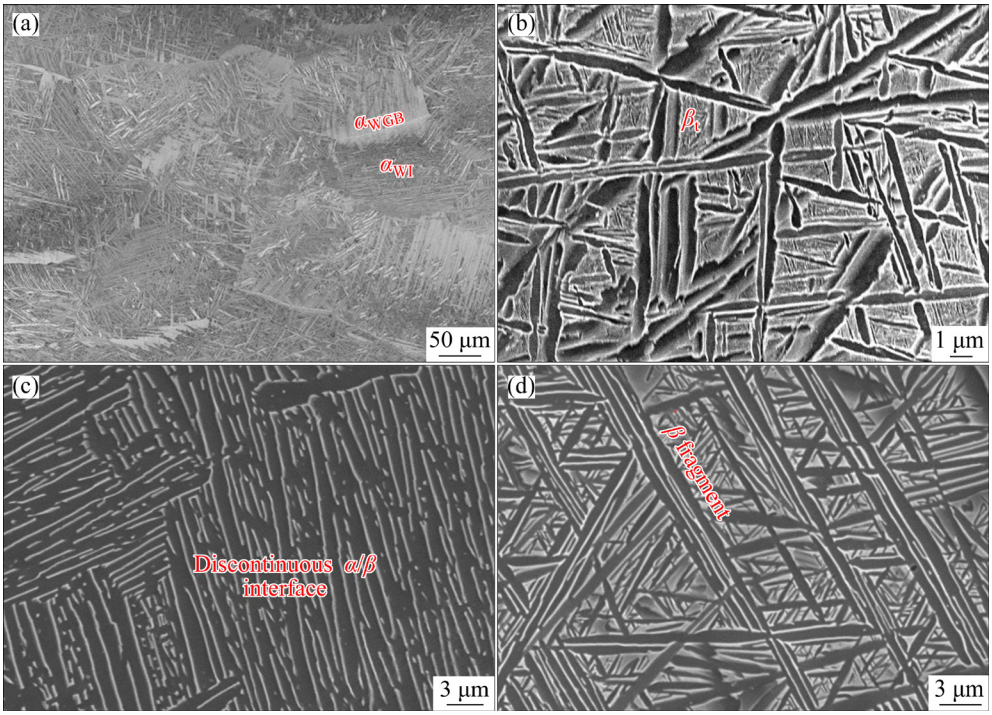

Fig. 3 OM (a) and SEM (b) images of as-extruded sample; SEM images of α_{WGB} (c) and α_{WI} (d) regions of 700-PM-PE sample

in the α_{WI} regions, as shown in Fig. 3(d). The as-extruded sample is mainly composed of α(H) phase, demonstrated by a significant broadening of the (0002) peak due to a certain amount of hydrogen atoms in the octahedral spaces, as shown in Fig. 4. After dehydrogenation annealing treatment, the XRD patterns reveal small peaks corresponding to the β phase at 2θ=39.14° and 56.54°, indicating a further decomposition of α(H) and subsequent formation of new α and β phases.

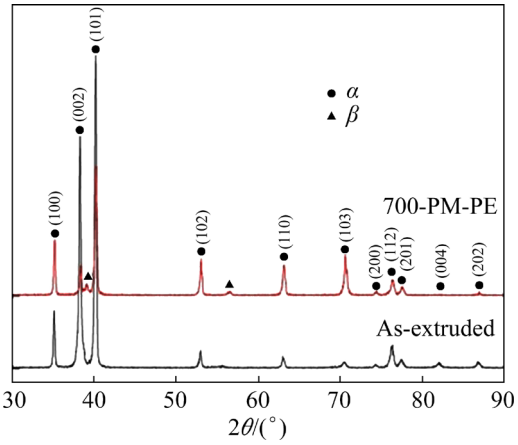

Fig. 4 XRD patterns of as-extruded sample and 700-PM-PE sample

The misorientation analysis results of the 700-PM-PE sample are shown in Fig. 5. A parent β grain is full of parallel α_{WGB} regions around grain boundaries and internal interwoven α_{WI} regions. Note that the α_{GB} regions become thin, short, and discontinuous in the 700-PM-PE sample, as shown in Fig. 5(a). The prior β-Ti grains are outlined by black lines based on the burgers orientation relationship (BOR) of $(0001)_\alpha//\{110\}_\beta$, as shown in Fig. 5(b). The grain size of prior β grain is above 110 μm, similar to that of the 700-PM-PF sample. Three typical orientational distributions of α_{GB} are detected. First, an independent thin α bar, marked by the red circle in Fig. 5(b), is obtained, because a new nucleation site is induced by the thorough decomposition of titanium hydrides. Second, based on the orientation of α_{WGB} on one side, the misorientation angle between the two adjacent parent β grains is less than 15°, as marked by the yellow circle in Fig. 5(b). Third, a few of the unified orientational microregions are attributed to the common $\{110\}_\beta$ of the two adjacent β grains, as marked by the green circle in Fig. 5(b). The corresponding pole point of $(0001)_\alpha$ strictly coincides with that of $\{110\}_\beta$, as demonstrated by the pole figure (PF) of Fig. 5(c).

Importantly, parts of α_{WGB} regions are replaced by interwoven fine α-laths, so that the area of α_{WGB} regions is much smaller than that of the vacuum sintered sample. All Euler maps of the subsets marked in Fig. 5(c) are shown in Figs. 5(d, e). The area proportions of these regions are 16.5% and 15.5%, respectively. In addition, the crystallographic orientations of the α_{WGB} regions are various. Most of the colonies exhibit discontinuous morphologies. Furthermore, the crystal orientations of the α_{WI} regions are multitudinous. Therefore, no special texture is detected in 700-PM-PE sample, as demonstrated by the PFs of $(0001)_\alpha$ in Fig. 5(c). This is in contrast to the $\langle 0001\rangle_\alpha$ micro-textured sample prepared by vacuum sintering and hot extrusion [29].

The proportions of high angle grain boundaries (HAGB, >15°) and low angle grain boundaries (LAGB, 2°−15°) are about 88.3% and 11.7%, respectively. The misorientation angles of adjacent grains are 0°, 10.5°, 60°, 63.5°, and 90°, in which the frequencies of 60° and 63.5° are relatively high due to the presence of α_{WI} regions. The next highest frequency is observed at 0°, owing to the α_{WGB} regions, as shown in Fig. 5(f). Approximately 23% of the α-grains characterized by uniformly distributed fragments inside the grain originate from recrystallization, as shown in Fig. 5(g). The main differences between the 700-PM-PF sample and the 700-PM-PE sample are the appearance of discontinuous α/β interfaces in the α_{WGB} regions, the orientational diversification of α-laths, and hierarchical interwoven nascent α aciculae in the α_{WI} sections of the 700-PM-PE sample, in terms of microstructural characteristics.

3.2 Tensile properties of samples with lamellar microstructure

The tensile properties of the two lamellar microstructure samples are displayed in Fig. 6. The 700-PM-PE sample with a discontinuous lamellar microstructure exhibits a UTS of (1080±5) MPa, a yield strength (YS) of (985±13) MPa, and an average EL of (13.6±1.8)%. In contrast, the as-forged 700-PM-PF sample with a regular fully lamellar microstructure renders reduced UTS (837±8) MPa, YS (814±5) MPa, and EL (10.0%) values [28]. Note that the strength and ductility are

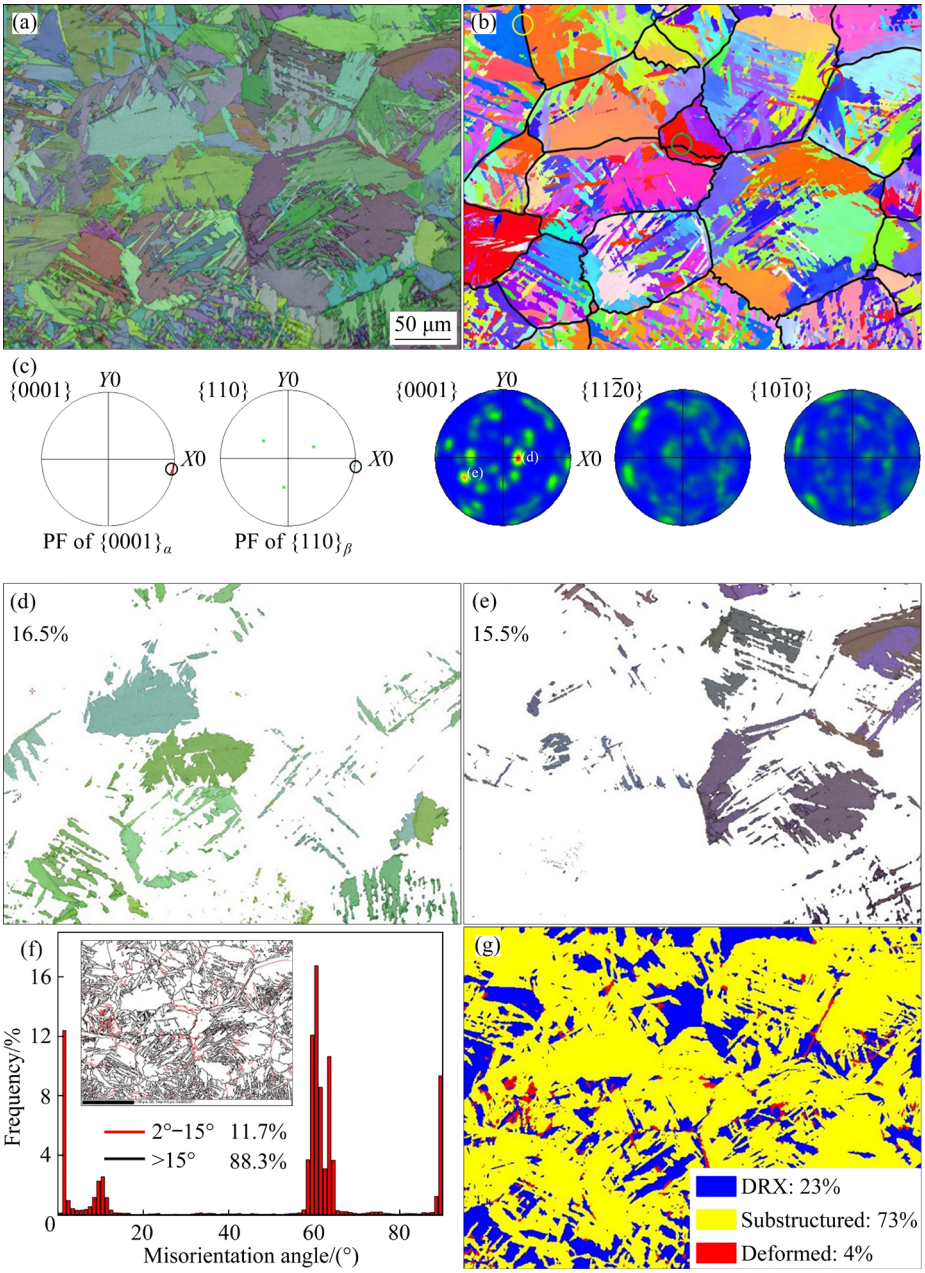

Fig. 5 EBSD results of 700-PM-PE sample: (a) All Euler map; (b) IPF map in extrusion direction; (c) PFs of green circle marked area and full area; (d, e) All Euler maps of subsets marked in (c); (f) Misorientation angle distribution map of α-Ti; (g) Recrystallization area

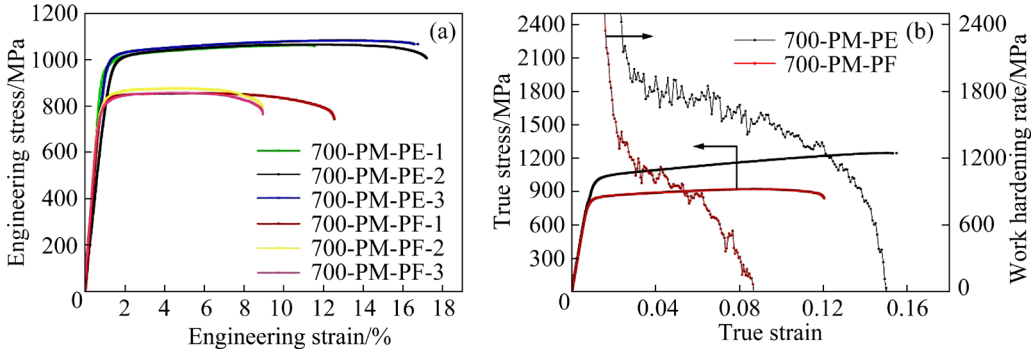

Fig. 6 Tensile properties of 700-PM-PE and 700-PM-PF samples: (a) Engineering stress−strain curves; (b) True stress−strain curves and work hardening rate curves

simultaneously improved in 700-PM-PE sample, as shown in Fig. 6(a). The UTS of the 700-PM-PE sample is 240 MPa higher than that of the 700-PM-PF sample in the case of maintaining a better tensile ductility. The true stress−strain and work hardening rate curves are shown in Fig. 6(b), where the uniform plastic deformation stage of the 700-PM-PE sample is located over 11.0% strain, while that of the 700-PM-PF sample stays at only 4.5% strain.

The DIC images and the corresponding strain distribution results along the gauge during tensile tests are shown in Fig. 7 to distinguish the degree of strain concentration. In the discontinuous lamellar microstructure of the 700-PM-PE sample, the area of the strain concentration region is always one quarter of the gauge section, which does not shrink significantly with the increase in strain, as shown in Fig. 7(a). The line strain (ε_{yy}) along the tensile direction is found to be relatively uniform up to 9.5% strain, as shown in Fig. 7(c). The final ε_{yy} value of 700-PM-PE sample is only 0.182 when the average tensile strain is 12%, implying the degree of strain concentration being 51%. By contrast, in the common lamellar microstructure of the 700-PM-PF sample, three strain concentration regions begin to shrink to two locations when the average tensile strain ranges from 0.7% to 9.5%, as shown in Fig. 7(b). Noticeable two peaks appear on the strain ε_{yy} curves at 4.3% strain, as displayed by Fig. 7(d), consistent with the above analysis result that deformation localization starts at low strain of 4.5% of the 700-PM-PF sample. Above 9.5% strain, one of the ε_{yy} strain peak values increases rapidly with increasing strain. The final ε_{yy} value reaches 0.47 locally when the average tensile strain is 12%, illustrating the degree of strain concentration being high (290%). It is established that the discontinuous lamellar microstructure of the 700-PM-PE sample improves the uniform plastic deformation ability and coordinated capability, effectively delays the deformation localization and avoids necking.

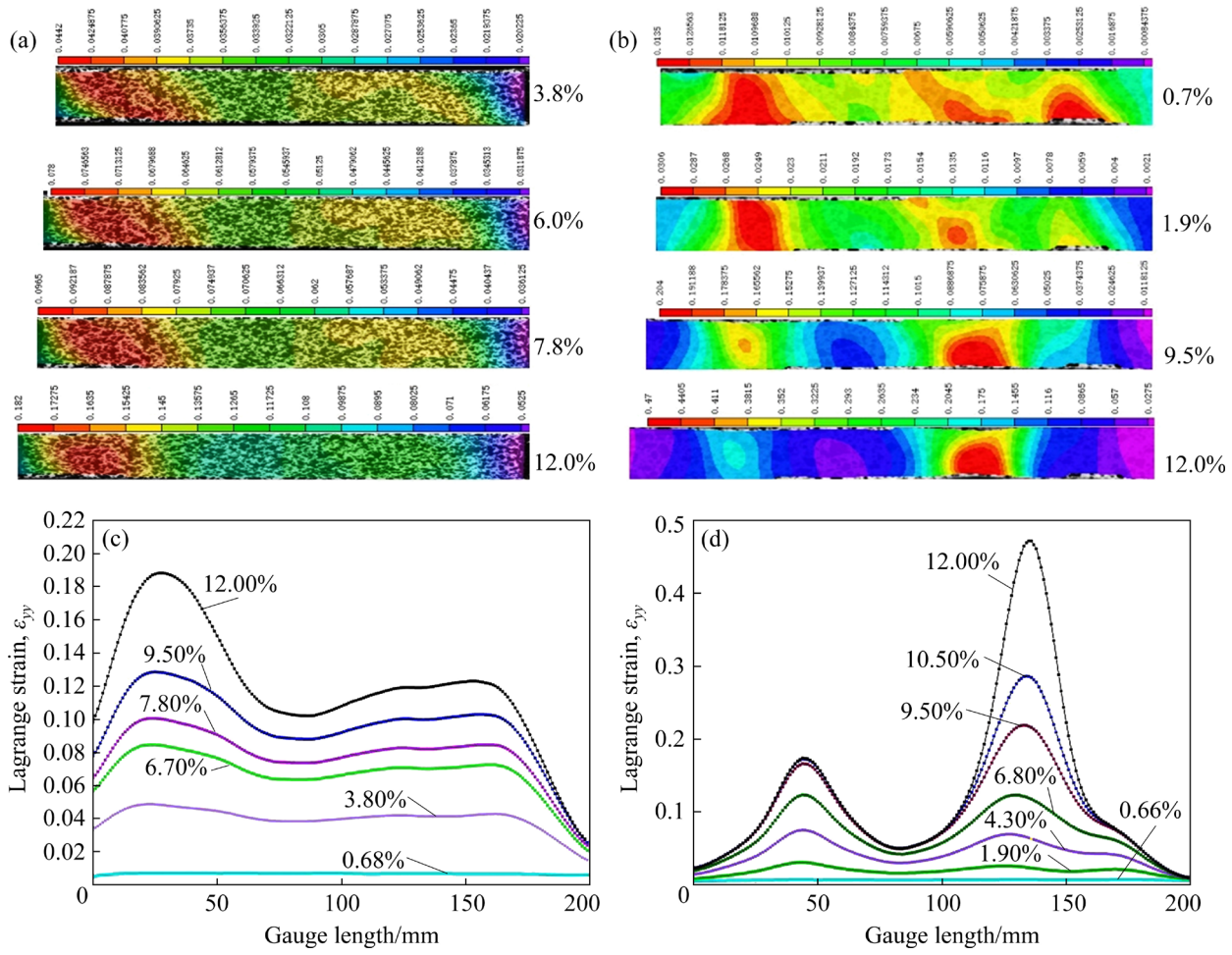

Fig. 7 Lagrange strain ε_{yy} maps (a, b), and strain ε_{yy} distribution diagrams along gauge section (c, d) of 700-PM-PE sample (a, c) and 700-PM-PF sample (b, d)

4 Discussion

4.1 Generation mechanism of discontinuous lamellar microstructure

It has been reported that the faster the heating rate, the more delayed the dehydrogenation process [30]. In addition, the rapid cooling rate after extrusion results in parallel α_{WGB} and interwoven α_{WI} regions in a single β parent grain. After induction sintering followed by immediate hot-extrusion by accelerating the heating rate and avoiding preservation at intense dehydrogenation temperature of 700 °C, 0.21 wt.% hydrogen content is remained. Thereby, hydrogen-rich phases, such as α(H) and β(H) phases and some acicular titanium hydrides are retained. The TEM results of as-extruded sample containing scanning transmission electron microscopy (STEM) images and bright field (BF) images are employed to further clarify the detailed characteristics, as shown in Fig. 8. Nanoscale β(H), β_t stripes full of nanoscale α aciculae and the retained TiH_x nucleating at the α/β_t interface are detected, as shown in Fig. 8(a). Fine α(H) laths occupied by some dislocations are present, indicating that the transformation of titanium hydrides to α(H) induces many crystal defects, as displayed in Fig. 8(b). Some acicular titanium hydrides are retained in the α(H) laths, and the interfaces of the secondary nanoscale α embedded in the β_t domains become blurred in Fig. 8(c). Moreover, α laths are detected to be obviously Ti and Al rich, and Mo depleted, while β strips are Ti and Al depleted, and Mo rich.

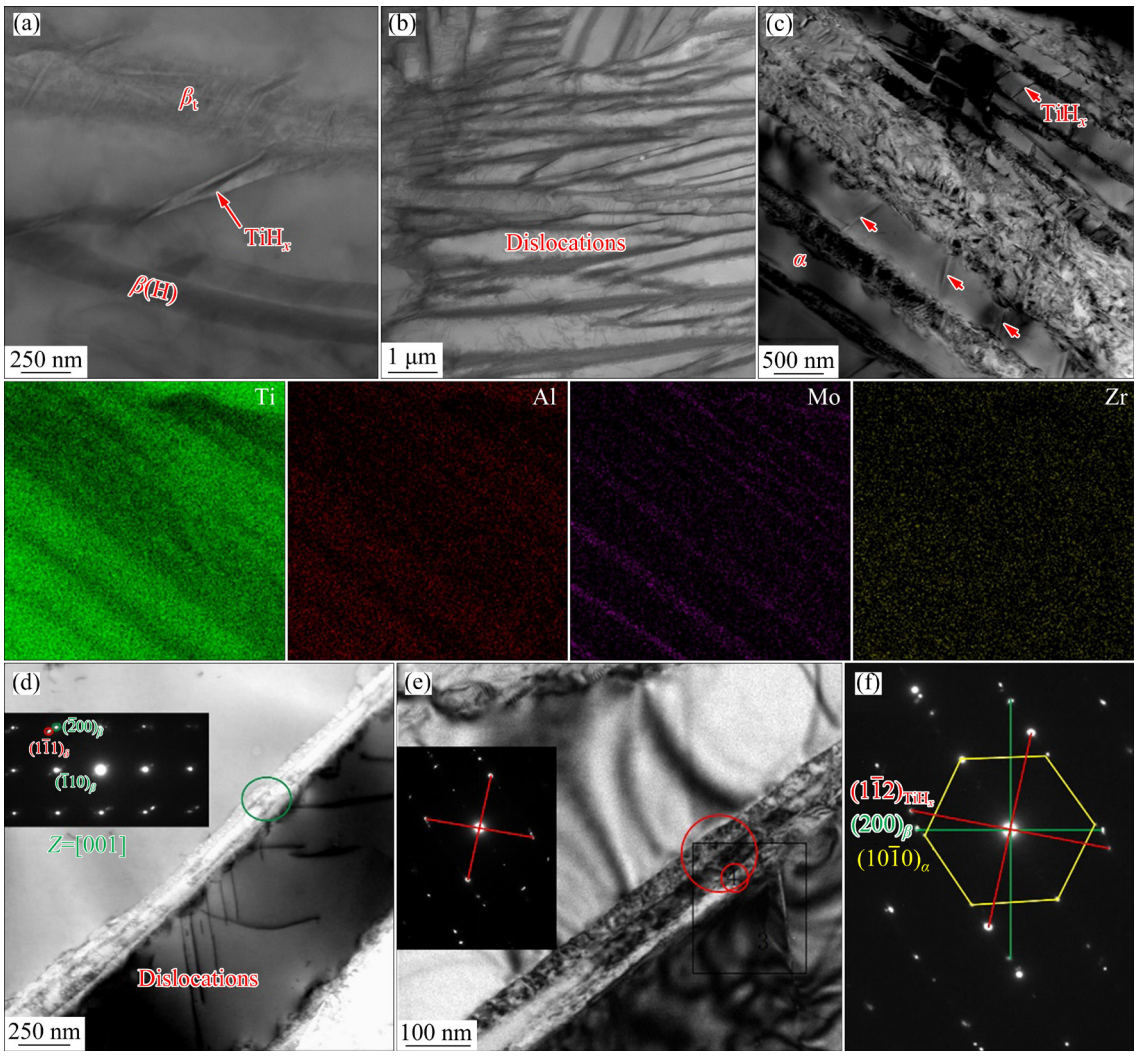

Fig. 8 Microstructure of as-extruded sample: (a−c) STEM images and corresponding elemental distribution maps of (c); (d, e) BF images showing interfacial phase and SAED pattern of small red circle; (f) SAED pattern of area marked by big red circle in (e)

In contrast, β_t domains are slightly Mo rich, and Ti and Al depleted. In addition, nanoscale titanium hydride strips with FCC structure accompanied by dislocations are found between the α and β stripes, as displayed in Figs. 8(d−f). The selected area electron diffraction (SAED) patterns shown in Fig. 8(d) demonstrate a slight deviation between $(200)_\beta$ and $(1\,\bar{1}\,1)_\delta$, unlike the $(200)_\beta // (1\,\bar{1}\,1)_L$ in the Ti−6Al−4V deposited sample by a diode laser cladding [23,31].

After dehydrogenation annealing, multiple dehydrogenation reactions of the hydrogen-rich β(H) stripes and interwoven α(H) aciculae, i.e., $\beta(H) + \alpha(H) + TiH_x \rightarrow \alpha + \beta + H_2$, are performed. Phase transitions are complex owing to the similar formation energies of various metastable phases during vacuum annealing [32]. From the TEM images of the 700-PM-PE sample in Figs. 9(a−f), the dislocations in the α-laths disappear after dehydrogenation annealing, but the nanoscale FCC-structured titanium hydrides (δ-TiH) between the α and β phases remain observable. The width of the δ-TiH phase is measured to be about 45 nm. Further transformation of the hydrogen-rich β-strips to nascent α brings about the broadening of α-laths and the discontinuities of β-strips in the localized regions, as marked by the yellow dotted circle in Figs. 9(g, h). Many new nanoscale interwoven α grains with widths of 50−80 nm precipitate in the α_{WI} regions, and the α/β interfaces become clear, as shown in Fig. 9(i). Further decomposition of the retained titanium hydrides and hydrogen-rich phases as well as many dislocations resulting from the above reactions contributes to the nucleation of new nanoscale α-laths and the discontinuities of the β-strips, as discussed in extra-low oxygen titanium alloys [33]. This is in contrast to the process of vacuum sintering to directly obtain α and β phases. Multiple phase transitions of the retained α(H) and β(H) phases are performed during the vacuum annealing treatment, which is favorable for the fabrication of hierarchical α structures.

It is worth noting that nanoscale FCC-structured layers between the α-laths and β-strips are retained after complete dehydrogenation annealing, to form an $\alpha/\delta/\beta$ structure. It has been

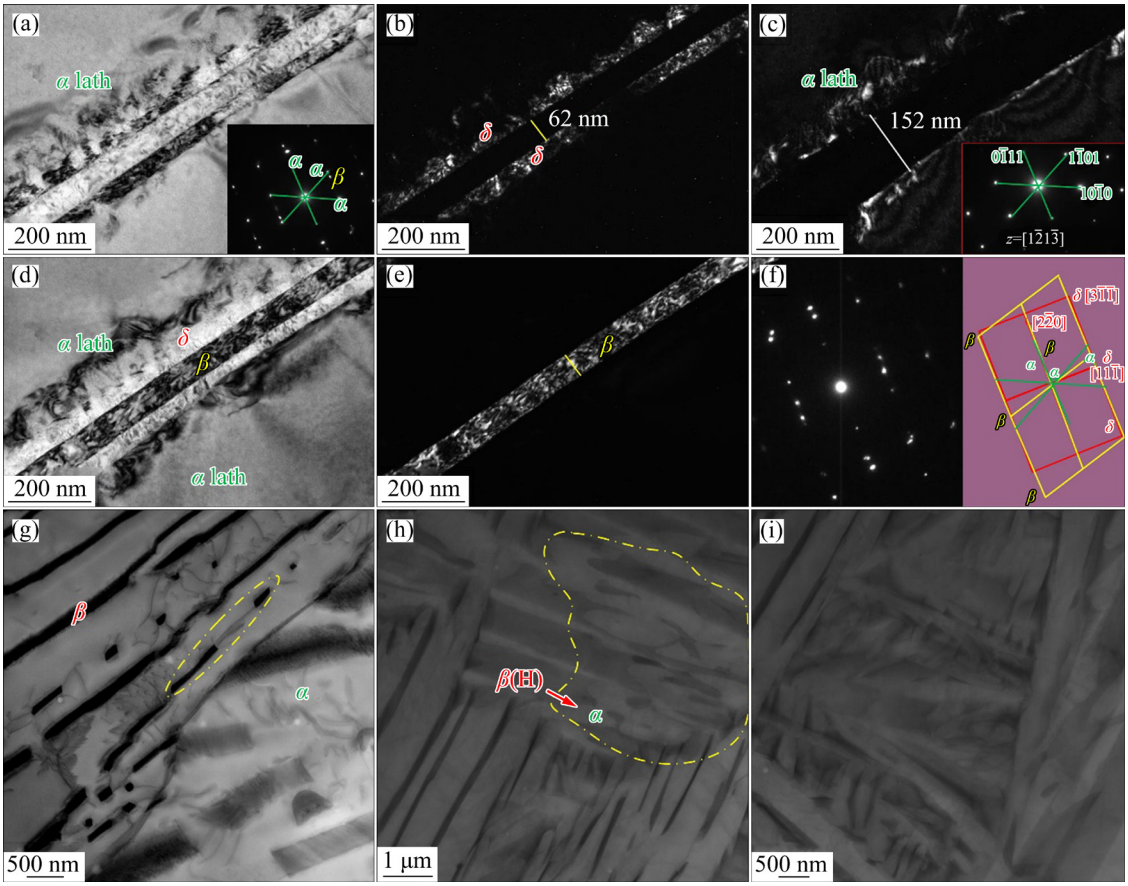

Fig. 9 TEM images of 700-PM-PE sample: (a−e) Characteristics of interfacial phase; (f) SAED pattern; (g−i) STEM images of discontinuous lamellar structures

reported that the interfacial layer was the result of 16 at.% V enrichment at the front of the β phase and a shear mismatch between α and β phases in Ti−6Al−4V alloy [34]. Otherwise, the FCC-structured interfacial layer acted as a transition in the striated form owing to the high V content during continuous cooling from the single β-phase field. Subsequently, a (111) twin was modified in the interfacial layer and then transformed into a hexagonal close-packed (HCP) α-phase equilibrium [35]. In this study, obvious Al, Mo depletion is observed in the nanoscale FCC-structured δ layers, and the Ti content of the interfacial δ layers is smaller than that of the α-laths, as displayed in Fig. 10. The difference of elemental compositions between the interface layers and the α-laths indirectly demonstrates that the interface layers belong to the residual titanium hydrides (δ-TiH), different from the report on high-oxygen Ti−6Al−4V alloy [5]. No classic Burgers relationship is found, in contrast to the interfacial phase resulting from the segregation of V at the front of the β-phase [31].

Complex dehydrogenation phase transitions resulting from β(H)/α(H) to α and β phases accompanied by recrystallization are carried out during vacuum annealing, which contributes to breaking the traditional interfacial growth law. Subsequently, the formation of continuous coarse α_{GB} plates at prior β grain boundaries is inhibited and the production of large α_{WGB} regions throughout the β parent grain is avoided. Consequently, a discontinuous lamellar microstructure consisting of discontinuous α_{GB}, α_{WGB} with $\alpha/\delta/\beta$ interface structure and interwoven α_{WI} regions is the characteristic of the 700-PM-PE sample. The dehydrogenation annealing at 700 °C brings about microstructural refinement and diversification of the α-variants inside the β parent grain.

4.2 Origin of high strength and good ductility of 700-PM-PE sample

The enhanced strength and good ductility of the 700-PM-PE sample can be ascribed to the high work hardening rate. As mentioned above, the uniform plastic deformation ability of the 700-PM-PE sample is twice as high as that of the 700-PM-PF sample. To further clarify the deformation behavior of the 700-PM-PE sample, the dislocations are examined by TEM, as shown in Fig. 11. The retained nanoscale δ-TiH between the α and β interfaces effectively hinders dislocation slipping. Additionally, obvious dislocation pile-ups at the $\alpha/\delta/\beta$ interface induce extra back stress, which activates different $\langle a \rangle$ slip systems in α-laths. Particularly, $\langle c+a \rangle$ pyramidal dislocations with high critical shearing stress are activated in some hard-orientation α-laths, which not only slip on the first pyramidal plane but also slip on the second pyramidal plane, as shown in Figs. 11(a−c). Dislocations slip primarily in the wavy and tangled form, as shown in Fig. 11(d). The dislocations of the discontinuous lamellar microstructure are blocked at the $\alpha/\delta/\beta$ interface, which is different from the dislocation transfer effect in common α/β interfaces [28]. In addition, shear bands in α-laths are broken at the $\alpha/\delta/\beta$ interface to avoid the formation of sample-scale cracks by connecting long shear bands, as shown in Fig. 11(e). The dislocation density increases with increasing the strain. No obvious long shear bands are observed due to the effective barrier of the $\alpha/\delta/\beta$ interface, and the dislocations are in the form of entanglements near the fracture, as shown in Fig. 11(f).

There is no dense twin substructure in the nanoscale interfacial layers because high oxygen content inhibits the formation of twins, which is different from the report [31]. The existence of the

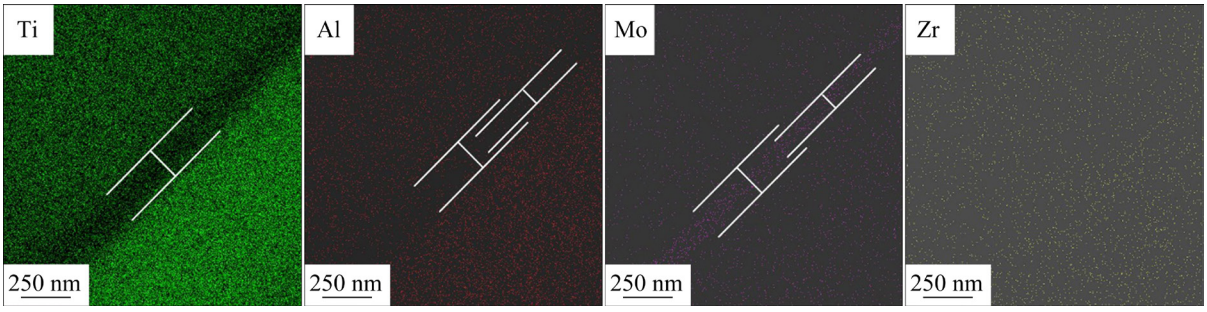

Fig. 10 Elemental mapping of $\alpha/\delta/\beta$ lamellar region in 700-PM-PE sample detected by TEM

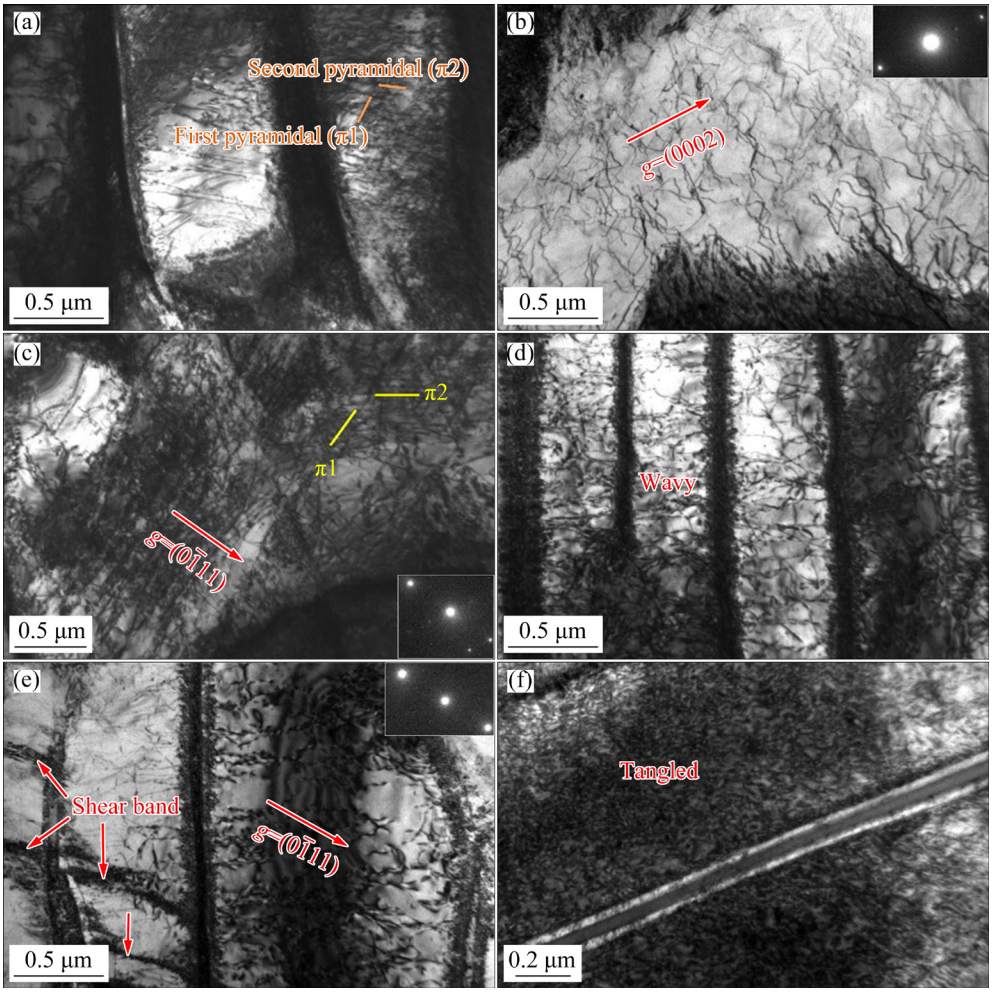

Fig. 11 BF-TEM images showing dislocations of tensile deformed 700-PM-PE specimen: (a−e) At 3.0% strain; (f) At strain close to fracture

$\alpha/\delta/\beta$ interface and the orientational diversification of the α-laths shorten the effective slip length of dislocations to the width of a single α-lath in the discontinuous lamellar microstructure of the 700-PM-PE sample. Therefore, the tensile strength is 240 MPa higher than that of the 700-PM-PF sample. The activation of multiple slip systems, particularly the first and second pyramidal $\langle c+a\rangle$ slip systems, provide the plastic deformation at the c-axis direction and promote the efficiency of wavy slip, which greatly enhances the work-hardening ability.

In polycrystalline samples, the coordinated deformation capabilities among various regions, especially the grain boundary layers, have a crucial effect on the fracture behavior. In the discontinuous lamellar microstructure, on the one hand, short and homogeneous microscale shear bands (MSBs) tilting about 45° to the tensile direction are interrupted by straight lands along the tensile direction, as shown by red dashed lines in Fig. 12(a). Microcracks are prone to form around boundaries when no visible MSBs are present on one side of the boundary, as shown in Fig. 12(a). Dispersed short MSBs are observed primarily in the α_{WI} regions and the propagation of MSBs inside the grain is terminated at the grain boundaries and the neighboring α_{WGB} regions, as shown in Figs. 12(b, c). The magnified view of α_{WGB} regions shown in Fig. 12(d) demonstrates that groups of parallel slip lines are present, which are arrested at the $\alpha/\delta/\beta$ interfaces and the boundaries with different orientational α_{WGB}. Therefore, no deep slip steps are visible in the α_{WGB} regions of Fig. 12(b). The formation of MSBs is considered to be associated with pyramidal $\langle a\rangle$ and $\langle c+a\rangle$ slips in some hard-oriented domains, while the slip bands are caused by basal and prismatic $\langle a\rangle$ slips, as

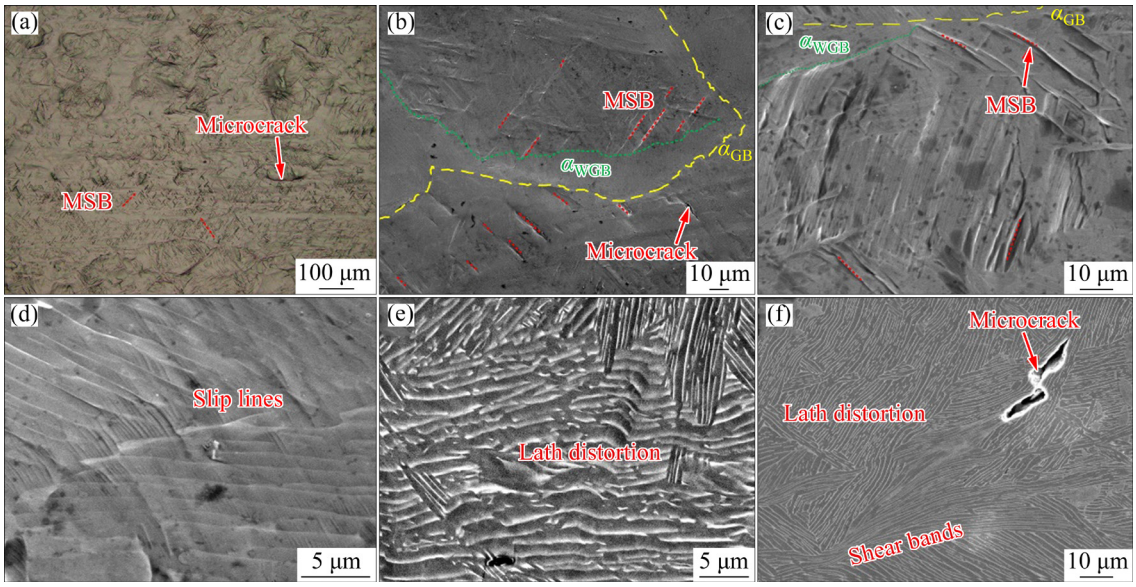

Fig. 12 Microstructure of longitudinal sections of tensile deformed 700-PM-PE sample: (a) Slip traces detected by OM; (b−d) SEM images showing MSBs and slip lines; (e, f) SEM images showing lath distortions, shear bands and microcracks

reported in Ref. [36]. On the other hand, lath distortions are performed to mitigate local stress concentration of discontinuous α/β interfaces in the α_{WGB} regions, as shown in Fig. 12(e). Shear bands and microcracks are generated at the boundaries of α_{WGB} with different orientations, as shown in Fig. 12(f). Therefore, multiple slip systems are activated in the tensile deformed 700-PM-PE sample. The combined effect of dispersed MSBs, short slip bands, shear bands and lath distortions mitigates the strain concentration and suppresses the microcracks from evolving into macroscale catastrophic premature cracks at the grain boundary.

5 Conclusions

(1) The dehydrogenation and a rapid cooling rate during fast sintering and hot extrusion result in a composite microstructure consisting of prior β-Ti grain boundary lamellar colonies (α_{WGB}) and internal interwoven hydrogen-rich α-laths (α_{WI}) and β_t matrix.

(2) Vacuum dehydrogenation annealing gives rise to a discontinuous fine lamellar microstructure containing $\alpha/\delta/\beta$ interfaces without special micro-texture. Particularly, the α_{GB} region becomes thin and polytropic.

(3) The discontinuous fine lamellar micro-structure renders a high UTS of 1080 MPa and a good EL of 13.6%. The tensile strength is 240 MPa higher than that of the counterpart with a regular lamellar microstructure, in the case that ductility is enhanced.

(4) The $\alpha/\delta/\beta$ interfaces prevent slipping transmission and contribute to the activation of multiple $\langle a \rangle$ and $\langle c+a \rangle$ slip systems, which enhances the work hardening rate. The combined effect of microscale shear bands, short slip bands, and lath distortion alleviates the stress concentration at grain boundaries and enhances compatible deformation capability.

CRediT authorship contribution statement

Hai-rui ZHANG: Conceptualization, Methodology, Investigation, Data curation, Writing − Original draft, Funding acquisition; **Hong-zhi NIU:** Supervision, Conceptualization, Funding acquisition; **Chao YANG:** Investigation; **Nang XIANG:** Investigation, Funding acquisition; **De-liang ZHANG:** Conceptualization, Supervision; **Fu-xiao CHEN:** Investigation.

Declaration of competing interest

The authors declare that they have no known competing financial interests or personal relationships that could have appeared to influence the work reported in this paper.

Acknowledgments

This work was financially supported by the National Natural Science Foundation of China (Nos. 52301145, 52275329), the Applied Basic Research Program of

Liaoning Province, China (No. 2023JH2/101300158), the Fundamental Research Fund for the Central Universities, China (No. N2202010), and the Key Research Programs of High Education Institutions in Henan Province, China (No. 24A430017).

References

[1] BANERJEE D, WILLIAMS J C. Perspectives on titanium science and technology [J]. Acta Materialia, 2013, 61: 844−879.

[2] CHEN T, SURYANARAYANA C, YANG C. Advanced titanium materials processed from titanium hydride powder [J]. Powder Technology, 2023, 423: 118504.

[3] ZHAO Qin-yang, CHEN Yong-nan, XU Yi-ku, TORRENS R, BOLZONI L, YANG Fei. Cost-affordable and qualified powder metallurgy metastable beta titanium alloy by designing short-process consolidation and processing [J]. Materials & Design, 2021, 200: 109457.

[4] FANG Z Z, PARAMORE J D, SUN Pei, CHANDRAN K S R, ZHANG Ying, XIA Yang, CAO Fei, KOOPMAN M, FREE M. Powder metallurgy of titanium−Past, present, and future [J]. International Materials Reviews, 2017, 63: 407−459.

[5] YAN Ming, DARGUSCH M S, EBEL T, MA Qian. A transmission electron microscopy and three-dimensional atom probe study of the oxygen-induced fine microstructural features in as-sintered Ti−6Al−4V and their impacts on ductility [J]. Acta Materialia, 2014, 68: 196−206.

[6] LUO Yi-fei, ZHANG Zhen, XIE Yue-huang, LIANG Jia-miao, ZHANG De-liang. The role of nanoscale heterogeneous structure in simultaneously enhancing strength and ductility of high-oxygen Ti−6Al−4V alloy [J]. Powder Metallurgy, 2020, 64(2): 142−148.

[7] ZHENG Yi-feng, YAO Xun, SU Yong-jun, ZHANG De-liang. High strength titanium with a bimodal microstructure fabricated by thermomechanical consolidation of a nanocrystalline TiH_2 powder [J]. Materials Science and Engineering A, 2017, 686: 11−18.

[8] ZHANG Hai-rui, NIU Hong-zhi, ZANG Meng-chao, YUE Ju-kun, ZHANG De-liang. Microstructures and mechanical behavior of a near α titanium alloy prepared by TiH_2-based powder metallurgy [J]. Materials Science and Engineering A, 2020, 770: 138570.

[9] MA Guang-yu, DONG Shu-cheng, SONG Yu-chao, QIU Fu-cheng, SAVVAKIN D, IVASISHIN O, CHENG Tuo. Sustaining an excellent strength–ductility combination for Ti−6Al−4V alloy prepared from elemental powder blends [J]. Journal of Materials Research and Technology, 2023, 23: 4965−4975.

[10] SONG Yu-chao, MA Guang-yu, QIU Fu-cheng, STASIUK O, SAVVAKIN D, IVASISHIN O, XU Xiao-feng, CHENG Tuo. Nearly dense Ti−6Al−4V/TiB composites manufactured via hydrogen assisted BEPM [J]. Ceramics International, 2022, 48(8): 10902−10910.

[11] ZONG Ying-ying, HUANG Shu-hui, FENG Ying-juan, SHAN De-bin. Hydrogen induced softening mechanism in near alpha titanium alloy [J]. Journal of Alloys and Compounds, 2012, 541: 60−64.

[12] LI Xi-feng, XU Fang-fei, HU Lan, ZHU Fu-hui, CHEN Jun. Tensile deformation behavior of coarse-grained Ti-55 titanium alloy with different hydrogen additions [J]. Rare Metals, 2020, 40(8): 2092−2098.

[13] MEI Li-bo, WANG Chun-ming, WEI Yu-hang, XIAO Su-fen, CHEN Yun-gui. Effects of hydrogen content on powder metallurgy characteristic of titanium hydrides [J]. International Journal of Hydrogen Energy, 2018, 43(14): 7102−7107.

[14] MA Guang-yu, CHENG Tuo, JIA Hai-long, YUAN Long, IVASISHIN O M, SAVVAKIN D G. A novel method to fabricate high strength and ductility Ti−3Al−5Mo−4.5V alloy based on TiH2 and pre-hydrogenated master alloy powders [J]. Materials & Design, 2023, 227: 111791.

[15] LI Xi-feng, JIA Guo-peng, QU Feng-sheng, WU Hui-ping, CHEN Jun. Ultrafine grain refinement and superplasticity of Ti-55 alloy obtained by hydrogen absorption and desorption [J]. Journal of Materials Engineering and Performance, 2018, 27(7): 3472−3477.

[16] SUN Pei, FANG Z Z, KOOPMAN M, XIA Yang, PARAMORE J, RAVI CHANDRAN K S, REN Yang, LU Jun. Phase transformations and formation of ultra-fine microstructure during hydrogen sintering and phase transformation (HSPT) processing of Ti−6Al−4V [J]. Metallurgical and Materials Transactions A, 2015, 46(12): 5546−5560.

[17] PARAMORE J D, FANG Z Z, SUN Pei, KOOPMAN M, CHANDRAN K S R, DUNSTAN M. A powder metallurgy method for manufacturing Ti−6Al−4V with wrought-like microstructures and mechanical properties via hydrogen sintering and phase transformation (HSPT) [J]. Scripta Materialia, 2015, 107: 103−106.

[18] ZHANG Ya-jing, FANG Sheng-min, WANG Yi-ming, ZHANG De-liang. Enhancement of tensile strength and ductility of titanium with a bimodal structure [J]. Materials Science and Engineering A, 2021, 803: 140701.

[19] LI Chang-yuan, LIU Chang-meng, LU Tao, GUO Yue-ling, LIU Bin. In-situ preparation of high oxygen content titanium via wire arc additive manufacturing with tunable mechanical properties [J]. Transactions of Nonferrous Metals Society of China, 2024, 34(1): 171−183.

[20] WU Xiao-gang, ZHANG Bo-wen, ZHANG Yan-hu, NIU Hong-zhi, ZHANG De-liang. Correlation between microstructures and tensile deformation behavior of a PM near α Ti−6Al−2Sn−4Zr−2Mo−0.1Si alloy [J]. Materials Science and Engineering A, 2021, 825: 141909.

[21] MENG Lei, GAO Jing-bo, YUE Ju-kun, ZHANG Jing-fan, ZHAO Xiao-li, ZHANG De-liang. Stress-based fatigue behavior of Ti−6Al−4V alloy with a discontinuous lamellar microstructure fabricated by thermomechanical powder consolidation [J]. Materials Science and Engineering A, 2020, 798: 140085.

[22] SHARMA B, VAJPAI S K, AMEYAMA K. Preparation of strong and ductile pure titanium via two-step rapid sintering of TiH2 powder [J]. Journal of Alloys and Compounds, 2016, 683: 51−55.

[23] ZHANG Bo-wen, LIU Zhu-jun, WU Xiao-gang, ZHANG De-liang. Sustaining an excellent strength-ductility combination of a PM α+β titanium alloy with fine prior β grains and heterogeneous microstructure [J]. Journal of Alloys and Compounds, 2022, 926: 166736.

[24] QIAN Jian-hang, WANG Ke-huan, ZENG Yuan-song, FU Ming-jie, WANG Fu-xin, LIU Gang. Microstructural evolution and mechanical properties of high-temperature pack rolled TiB_w/TA15 composite sheets with network structure [J]. Transactions of Nonferrous Metals Society of China, 2023, 33(12): 3699−3711.
[25] TEIXEIRA J C D, APPOLAIRE B, AEBY-GAUTIER E, DENIS S, BRUNESEAUX F. Modeling of the effect of the β phase deformation on the α phase precipitation in near-β titanium alloys [J]. Acta Materialia, 2006, 54: 4261−4271.
[26] FAN Wei, PENG Yi-jie, WANG Yong-xia, QI Yang, FENG Zhe, TAN Hua, ZHANG Feng-ying, LIN Xin. Effect of grain boundary Widmanstätten α colony on the anisotropic tensile properties of directed energy deposited Ti−6Al−4V alloy [J]. Journal of Materials Science & Technology, 2023, 184: 145−156.
[27] SUN Zhi-chao, GUO Shuang-shuang, YANG He. Nucleation and growth mechanism of α-lamellae of Ti alloy TA15 cooling from an α+β phase field [J]. Acta Materialia, 2013, 61: 2057−2064.
[28] ZHANG Hai-rui, NIU Hong-zhi, ZHANG Yan-hu, ZANG Meng-chao, ZHANG De-liang. Achieving a high strength and tensile ductility synergy of a high-oxygen powder metallurgy near alpha titanium alloy by importing β_t domains into lamellar structures [J]. Journal of Alloys and Compounds, 2022, 894: 162517.
[29] ZHANG Hai-rui, NIU Hong-zhi, LIU Shun, ZANG Meng-chao, ZHANG De-liang. Significantly enhanced tensile ductility and its origin of a ⟨0001⟩ micro-textured extrusion bar of a powder metallurgy near alpha titanium alloy [J]. Scripta Materialia, 2022, 213: 114633.
[30] MIDDLEMAS S, FANG Z Z, FAN P. A new method for production of titanium dioxide pigment [J]. Hydrometallurgy, 2013, 131/132: 107−113.
[31] ZHAO Zhuang, CHEN Jing, GUO Shuai, TAN Hua, LIN Xin, HUANG Wei-dong. Influence of α/β interface phase on the tensile properties of laser cladding deposited Ti−6Al−4V titanium alloy [J]. Journal of Materials Science & Technology, 2017, 33: 675−681.
[32] SHEN Chun-lei, LIU Yi, GONG Yu-xiang, LIU Zheng-qing, JIANG Yong, XU Can-hui, ZHOU Xiao-song, LONG Xing-gui. Environment-dependent phase stabilities of titanium hydrides: First-principles prediction [J]. Transactions of Nonferrous Metals Society of China, 2023, 33(10): 3017−3026.
[33] ZHANG Hai-rui, NIU Hong-zhi, ZANG Meng-chao, ZHANG Yan-hu, LIU Shun, ZHANG De-liang. Tensile properties and deformation behavior of an extra-low interstitial fine-grained powder metallurgy near alpha titanium alloy by recycling coarse pre-alloyed powder [J]. Journal of Materials Science & Technology, 2022, 129: 96−107.
[34] TAN Xi-peng, KOK Y, TAN Yu-jun, DESCOINS M, MANGELINCK D, TOR S B, LEONG K F, CHUA C K. Graded microstructure and mechanical properties of additive manufactured Ti−6Al−4V via electron beam melting [J]. Acta Materialia, 2015, 97: 1−16.
[35] RHODES C G, PATON N E. Formation Characteristics of the α/β interface phase in Ti−6Al−4V [J]. Metallurgical and Materials Transactions A, 1979, 10A: 209−216.
[36] LIU Zhi-ying, LI Ren-kai, CHEN Dao-lun, SUN Yu, HE Bei, ZOU Yu. Enhanced tensile ductility of an additively manufactured near-α titanium alloy by microscale shear banding [J]. International Journal of Plasticity, 2022, 157: 103387.

TiH_2 基粉末冶金钛合金不连续片层组织的强塑性机制

张海瑞[1,2]，牛红志[3]，杨 超[4]，相 楠[1,2]，张德良[3]，陈拂晓[1,2]

1. 河南科技大学 材料科学与工程学院，洛阳 471023；
2. 有色金属新材料与先进加工技术省部共建协同创新中心，洛阳 471023；
3. 东北大学 材料科学与工程学院，沈阳 110819；
4. 上海交通大学 材料科学与工程学院，上海市先进高温材料与精密成形重点实验室，上海 200240

摘 要：采用 TiH_2 基粉末冶金技术制备了具有不连续片层组织的钛合金，片层组织由母相 β 晶界附近平行的 α 晶团和晶内交织的 α 板条组成。在 700 ℃真空退火过程中，α 变体取向变得多样化，形态上呈现不连续性。α 和 β 条带之间产生纳米级界面相 δ-TiH，在拉伸变形过程中使位错在 $\alpha/\delta/\beta$ 界面处堆集，滑移带的长度缩短至单个 α 条的宽度，多种⟨a⟩型滑移尤其是锥面⟨c+a⟩滑移被激活，促进位错的波滑移，提高加工硬化率。在分散的微剪切带和板条扭曲的共同作用下，晶界处的应力集中得到缓解。最终，样品的极限抗拉强度为 1080 MPa，断裂伸长率为 13.6%，实现了高氧含量钛合金的强塑性匹配。

关键词：氢化钛基粉末冶金；不连续片层组织；界面 δ-TiH 相；拉伸性能；变形行为

(Edited by Bing YANG)